Aerodynamic loads on cactus-shaped cylinders at low Reynolds numbers

Pradeep Babu and Krishnan Mahesh[a)]
Department of Aerospace Engineering and Mechanics, University of Minnesota, Minneapolis, Minnesota 55455, USA

(Received 21 September 2007; accepted 15 January 2008; published online 31 March 2008)

Direct numerical simulations of flow past cactus-shaped cylinders are performed at Reynolds numbers of 20, 100, and 300. The results are contrasted to those from smooth cylinders at the same Reynolds numbers. The cavities in the cactus-shaped cylinders are seen to reduce the forces acting on them. At Reynolds number of 20, the drag is reduced by 22% due to reduction in the viscous forces. At Reynolds number of 100, the unsteady pressure forces increase, while the unsteady viscous forces acting on the cactus-shaped cylinder decrease. The overall reduction in drag force is about 18%. At Reynolds number of 300, onset of three dimensionality is observed together with significant decrease in pressure and viscous forces. Both the mean and fluctuating forces are found to decrease considerably. The Strouhal number is also found to decrease by about 10%. These reductions in force magnitudes and observed wake instabilities are attributed to the presence of large-scale, quiescent, recirculating flow within the cactus cavities. © *2008 American Institute of Physics*. [DOI: 10.1063/1.2887982]

I. INTRODUCTION

The motivation for this work is provided by the Saguaro species of cacti, which are found in desert regions. These cacti grow up to 50 ft in height[1] and have shallow root systems which span less than 1 ft. In spite of their shallow root system, the Saguaro cacti are able to withstand very high wind velocities (Reynolds number $\sim 10^6$). The impact of shape of the cacti on their aerodynamics has been of interest to biologists for many years.[2] Niklas and Buchman[3] observed that the h/D aspect ratio (total height of cacti above ground/maximum diameter of cross section) is dependent on cactus height. Saguaro cacti which are more than 15 ft in height have an h/D ratio between 12 and 23 while more slender Saguaro cacti have a much lower h/D ratio (5–12). Typical diameters of these cacti are about 1.5 ft. Also the cross section of the Saguaro trunk is characterized by longitudinal cavities, with spines at the tips of the cavities. Hodge[1] observed that the number of cavities on the surface vary between 10 and 30 depending on the age and height of the cacti. If l is the height of the spike, a 5 ft cactus has an average cavity depth of 0.07 ± 0.0015 (Ref. 2). As the cactus grows, the number of cavities and cavity depth change to maintain this average cavity depth. Talley and Mungal[4] observed that the cavity depth may increase in regions higher up the trunk.

Studies have been performed[1,3,5–7] to determine the effect of structural properties on the ability of Saguaro cacti to withstand high wind velocities. Saguaros appear to have low structural strength given that their stems contain up to 95% water.[5] They use few hard wood tissues to support their height. The center of the stem contains xylem fibers which have less than half the density and specific stiffness of solid wood.[3] Another observation concerns the evolution of two cacti families found in the Americas and in Africa. Gibson and Nobel[5] have observed that the Cactaeceae of the Americas and the Euphorbiaceae of South Africa have evolved independently but have a common body structure. They are characterized by longitudinal cavities which grow along their trunk and have spines at the tip of the cavities. It is speculated that the combination of these longitudinal cavities together with the spines help in reducing the fluctuating aerodynamic loading acting on the cactus at high wind velocities.

Talley *et al.*[8] and Talley and Mungal[4] have performed experiments at high Reynolds numbers $(2\times10^4-2\times10^5)$ to study the aerodynamics of cactus surface geometry for different cavity depths. Experimental studies were performed using cylinders with uniform surface roughness $(k_s/D=1.74\times10^{-3}, 8.41\times10^{-3})$ and cylinders with cavities. A total of 24 V-shaped cavities were considered for three different cavity depths ($L/D=0.035$, 0.07, and 0.105). Their results conclusively showed that cavities produce a dampening effect on the fluctuating drag and lift forces. Cylinders with cavities were found to have higher negative pressures on the sides of the cylinder. This behavior was insensitive to cavity depth. On the other hand, pressure recovery appeared to increase with increasing depth of the cavities. In the range of Reynolds numbers considered, Talley and Mungal[4] found that the presence of cavities resulted in consistent reduction of C_D for two-dimensional and free-ended cylinders. They speculate that a lower variation of $\partial C_D/\partial \mathrm{Re}$ for a cactus-shaped cylinder than a smooth cylinder may be biologically important for the survival of the species, since this would reduce the steep variation in forces acting on the smooth cylinder due to varying wind velocities.

The present work is directed toward understanding the nature of aerodynamics in various flow regimes for a smooth cylinder and a cactus-shaped cylinder. Direct numerical simulations are performed for a smooth cylinder and a cactus-shaped cylinder at three Reynolds numbers corresponding to different flow regimes; 20 (laminar), 100 (two-

a)Author to whom correspondence should be addressed. Electronic mail: mahesh@aem.umn.edu. Telephone: 612 624 4175. Fax: 612 626 1558.

 © 2008 American Institute of Physics

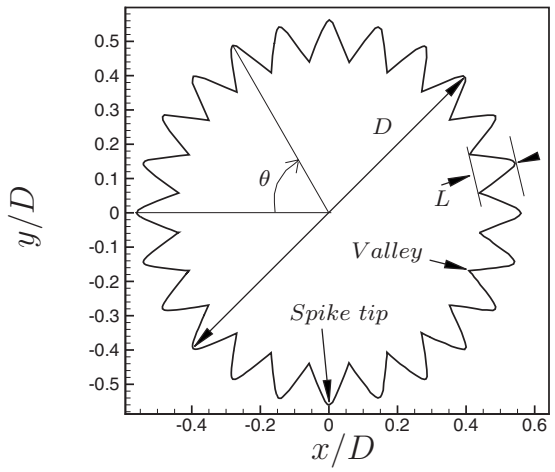

FIG. 1. Schematic of the cactus cross section. Note the θ starts from the leading edge and is along the clockwise direction. This convention is used for sake of clarity in ensuing discussions.

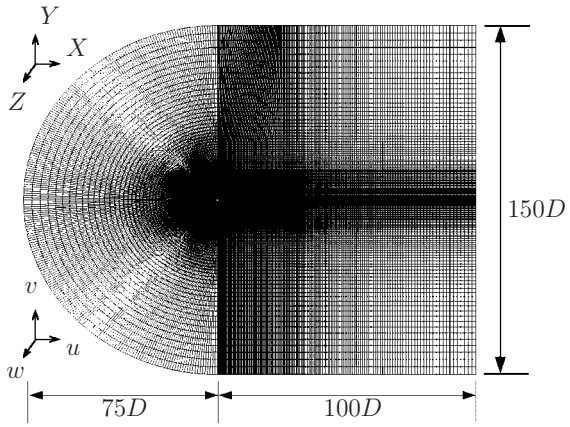

FIG. 2. Domain used for simulations.

dimensional and unsteady), and 300 (three-dimensional and transitional/turbulent). The fluctuating drag and lift forces are computed and their basic nature is examined at these Reynolds numbers. A qualitative mechanism for drag reduction and its dependence on the nature of grooves in cactus geometry is presented. The paper is organized as follows: Sec. II presents relevant simulation details and Sec. III discusses results performed at three different Reynolds numbers. Section IV summarizes the drag reduction mechanism observed at various Reynolds numbers, and discusses fluctuating force variation at higher Reynolds numbers.

II. SIMULATION DETAILS

The governing equations are the incompressible Navier–Stokes equations,

$$\frac{\partial u_i}{\partial x_i} = 0, \quad \frac{\partial u_i}{\partial t} + \frac{\partial u_i u_j}{\partial x_j} = -\frac{1}{\rho}\frac{\partial p}{\partial x_i} + \nu\frac{\partial^2 u_i}{\partial x_j \partial x_j}, \tag{1}$$

where u_i, p, ρ, and ν denote the velocity, pressure, density, and kinematic viscosity, respectively.

Direct numerical simulations were performed at three different Reynolds numbers, 20, 100, and 300. A Reynolds number of 20 corresponds to steady laminar flow, 100 to two-dimensional unsteady flow, and 300 to a transitional/turbulent flow field. The spike ratio (L/D) is defined as the ratio between the maximum height of the spike (L) to the total diameter (corresponding to outer radius, D) of the cylinder. Figure 1 shows the schematic of a cactus domain with these parameters. Simulations are performed for two different cylinder geometries with spike ratios equal to 0 and 0.105. L/D of 0 corresponds to a smooth cylinder while 0.105 corresponds to a cactus-shaped cylinder. Figure 2 shows a schematic of a radial cross section of the domain used. A Cartesian coordinate system is used such that the free-stream flow is along the X direction, and the span is along the Z direction. The velocities corresponding to X, Y, and Z are u, v, and w. Note that the computational domain extends to $75D$ upstream of the cylinder and $100D$ downstream. The radial domain ($\pm Y$ direction and perpendicular to free-stream) spans to $75D$ from the center of the cylinder.

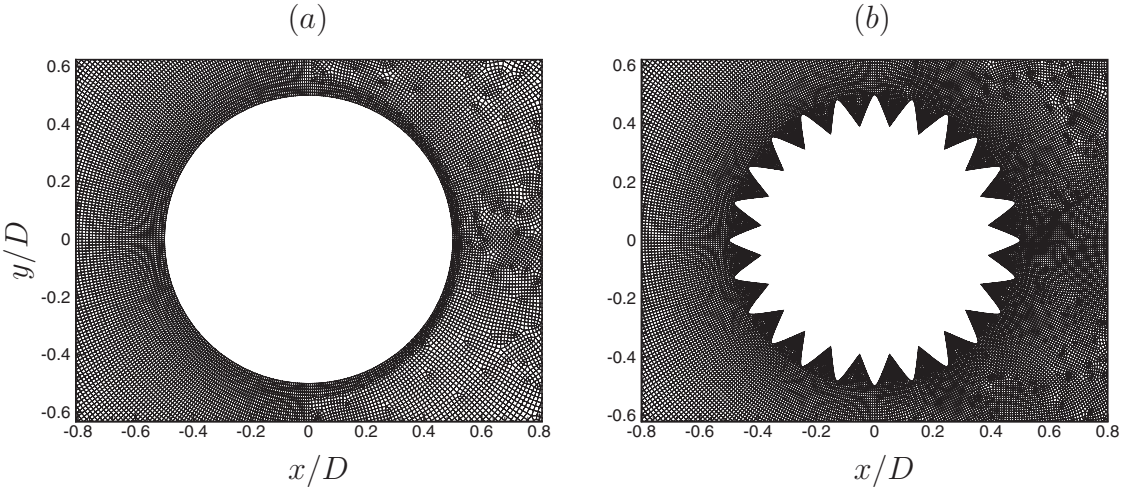

FIG. 3. Illustration of the grid in the vicinity of (a) smooth cylinder, and (b) cactus-shaped geometry.

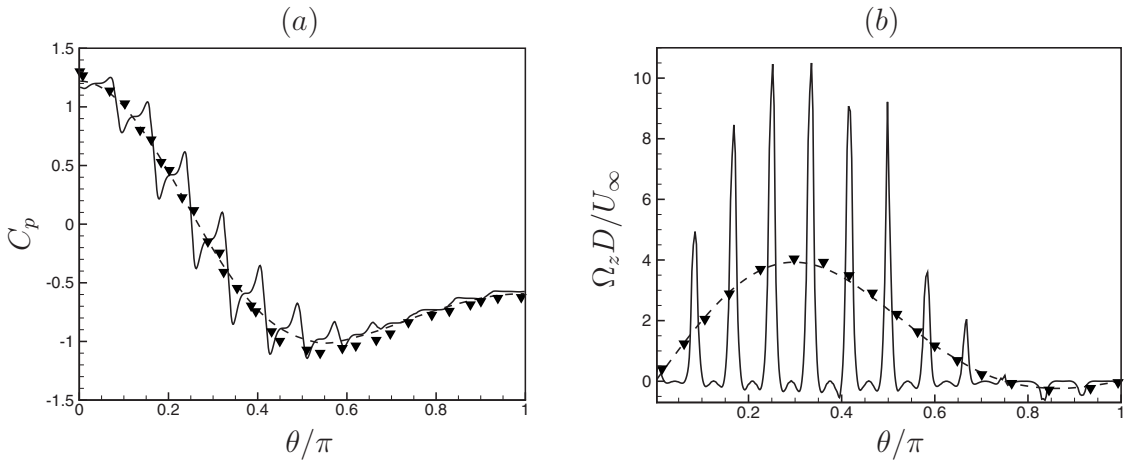

FIG. 4. Comparison results of (a) pressure coefficient C_p and (b) spanwise vorticity Ω_z at Re=20 for smooth cylinder and cactus-shaped cylinder. (—) Cactus, (---) cylinder, and (∇) Ref. 10.

Inflow boundary conditions are used for $x \leqslant 0$ and zero-gradient boundary conditions for $x > 0$.

Convective boundary conditions are used at the outflow boundaries and periodic boundary conditions are applied at the spanwise boundaries. The spanwise (z/D) domain is set to π and 32 planes are used for the turbulent flow simulations. Figures 3(a) and 3(b) show the unstructured hexahedral mesh elements used in the immediate vicinity of surface for the smooth cylinder and cactus-shaped cylinder, respectively. The unstructured capability helps in having high resolution elements in the vicinity of surface and in regions of interest while maintaining coarse elements in regions farther away from free-stream. Each plane consists of about 218 000 hexahedral elements. For the laminar calculations, the grid contains 436×10^3 hexahedral elements while the simulations at Reynolds number 300 contains about 7×10^6 hexahedral elements.

The numerical algorithm is described in detail by Mahesh *et al.*[9] and will only be summarized here. The algorithm is a predictor-corrector formulation that emphasizes discrete energy conservation for the convection and pressure terms on unstructured grids with arbitrary elements. The Cartesian components of velocity and pressure are stored at the centroids of the grid elements, and face-normal velocities are stored at the centroids of the faces. The nonlinear and viscous terms are used to obtain a predictor value for the cell-centered velocities. The predicted values of u_i are used to obtain predicted values for the face-normal velocities, which are then projected to obtain the pressure. Once the pressure is obtained, the Cartesian velocities are updated using a least-squares formulation for the pressure gradient. Time advancement scheme is implicit which uses the Crank–Nicholson approach. The algorithm has been validated for a variety of turbulent flows and is discussed in detail by Mahesh *et al.*[9]

Domain convergence studies were performed using a smooth cylinder at Reynolds number of 20. The total drag coefficient (C_D), pressure coefficient (C_p), and spanwise vorticity (Ω_z) were compared for various domain sizes. The pressure coefficient C_p is defined as $2(P-P_\infty)/\rho \cdot U_\infty^2$, where P is the pressure on the surface of the cylinder, P_∞ is the free-stream pressure, and U_∞ is the free-stream velocity. The drag coefficient is defined as $2(F_{\text{visc}}+F_{\text{press}})/\rho \cdot U_\infty^2 S_D$, where F_{visc} is the viscous force, F_{press} is the pressure force, and S_D is the surface area of the cylinder projected along the free-stream. Similarly, the lift coefficient $C_L=2(F_{\text{visc}}+F_{\text{press}})/\rho \cdot U_\infty^2 S_L$, where S_L is the projected surface area of the cylinder normal to the free-stream flow. These studies were performed such that the topology and size of grid elements in the vicinity of the cylinder was maintained constant while the domain size in the free-stream was increased. Three different studies were performed in which the domain size (upstream, radial, and downstream) were changed to $20D$, $75D$, and $160D$. The results were compared to the experimental results of Neuwstadt and Keller[10] and past computational results. The results from domain sizes $75D$ and $160D$ agree well with each other. There were differences in the C_D and C_L values between the $20D$ domain and $75D$ domain indicating flow confinement. Therefore simulations were performed on the $75D$ domain to obtain the results presented in this paper.

Grid convergence studies were also performed. For these studies, a cylinder with a domain size of $20D$ was used for the simulations. The resolution of the mesh in the vicinity of the cylinder was increased until a grid converged solution was obtained. On the surface of the cylinder and cactus geometry, the elements for the grid-converged solution are $0.0052D$ in the azimuthal direction and $0.006D$ radially. Therefore each cactus spike contain about 48 elements. The unstructured capability helps to contain the total number of

TABLE I. Comparison of loads acting on smooth cylinder and cactus-shaped cylinder at Re=20.

Steady loads	Cylinder	Cactus	% difference
Viscous drag coefficient	0.62	0.19	−69.35
Pressure drag coefficient	1.19	1.21	1.34
Total drag coefficient	1.81	1.40	−22.65

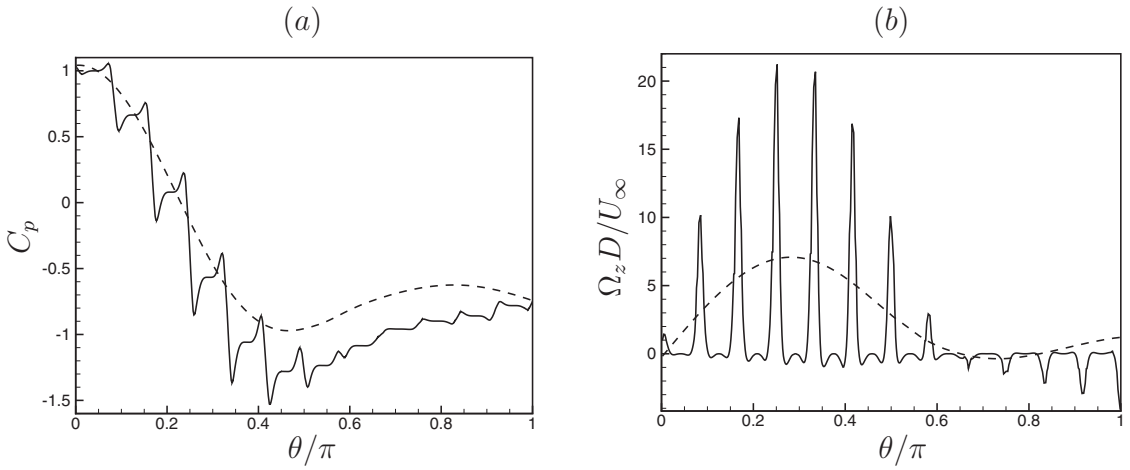

FIG. 5. Comparison of (a) pressure coefficient and (b) spanwise vorticity, at Re=100 for the smooth cylinder and the cactus-shaped cylinder. (—) Cactus and (---) cylinder.

elements while maintaining fine mesh elements in regions of interest. On the centerline at $2D$ downstream from the center of cylinder, the average element size is about $0.0082D$. At a distance of $10D$ downstream on the centerline, the average element size is about $0.1D$.

III. RESULTS

The results are divided into sections based on Reynolds number. The smooth cylinder is compared to the cactus geometry. Also, the results are compared to past simulation and experimental data.

A. Re=20

Figure 4(a) shows the pressure coefficient C_p as a function of the nondimensional azimuthal angle θ/π. In a two-dimensional flow, the viscous drag on the cylinder can be obtained from the spanwise vorticity. Therefore, vorticity results are shown in Fig. 4(b). Note that $\theta/\pi=0$ corresponds to the leading edge of the cylinder while $\theta/\pi=1$ corresponds to the trailing edge. The results from simulations are compared to the experimental data of Neuwstadt and Keller.[10] The results for the smooth cylinder from the present simulations agree well with the previous experimental results. While the pressure coefficient profiles for a smooth cylinder show a smooth variation, the profiles over the cactus-shaped cylinder shows sharp spatial variations consistent with the physical geometry.

The pressure coefficients shown in Fig. 4(a) are lowest at the tip of the spikes and largest at the valleys. Also, the spanwise vorticity [shown in Fig. 4(b)] on the cactus surface differs considerably from the smooth cylinder. The spanwise vorticity is minimum at the valleys (in between the spikes) and maximum at the tip of the spikes. This behavior in C_p and Ω_z is due to acceleration of the flow at the tips of the spikes and deceleration in the valleys. The interesting feature observed in these profiles is that although the local spanwise vorticity at the spikes for cactus-shaped cylinder is higher than the corresponding smooth cylinder, and the overall integrated effect of spanwise vorticity for a cactus-shaped cylinder is lesser than the smooth cylinder. This observation is reflected in the quantitative loads acting on the surface of the smooth cylinder and cactus-shaped cylinders. Table I shows a quantitative comparison of these results. It is seen that the presence of spikes reduces the viscous drag by about 69% while the pressure drag increases by more than 1.3%. These competing effects decrease the total drag by about 22%.

B. Re=100

Figure 5 shows the pressure coefficient and spanwise vorticity at Re=100. The flow is unsteady and therefore, the flow field is time averaged to obtain mean values. The qualitative trends are similar to the Reynolds number 20 simulations discussed in Sec. III A. Figure 5(a) shows higher pressure drop closer to the trailing edge due to the presence of spikes. Note in Fig. 5(b) that the maximum value of spanwise vorticity at the tip of the spikes of cactus-shaped cylinders is far greater than values obtained for the smooth cylinder. This relative difference is greater than what is observed at Reynolds number of 20, and translates quantitatively into an appreciable decrease in drag forces acting on the cactus-shaped cylinder. Table II shows these results. The presence of spikes on the surface of the smooth cylinder decreases the maximum viscous drag by more than 76% while the pressure drag increases by 2.0%. Similar to the unsteady drag forces, the viscous lift decreases by more than 66% while the

TABLE II. Comparison of loads acting on smooth cylinder and cactus-shaped cylinder at Re=100.

Unsteady loads	Cylinder	Cactus	% difference
Drag coefficient (max)	1.35	1.10	−18.52
Pressure drag (max)	1.00	1.02	2.00
Viscous drag (max)	0.34	0.08	−76.47
Lift coefficient (max)	0.33	0.30	−9.09
Pressure lift (max)	0.28	0.28	0.0
Viscous lift (max)	4.5×10^{-2}	1.5×10^{-2}	−66.67

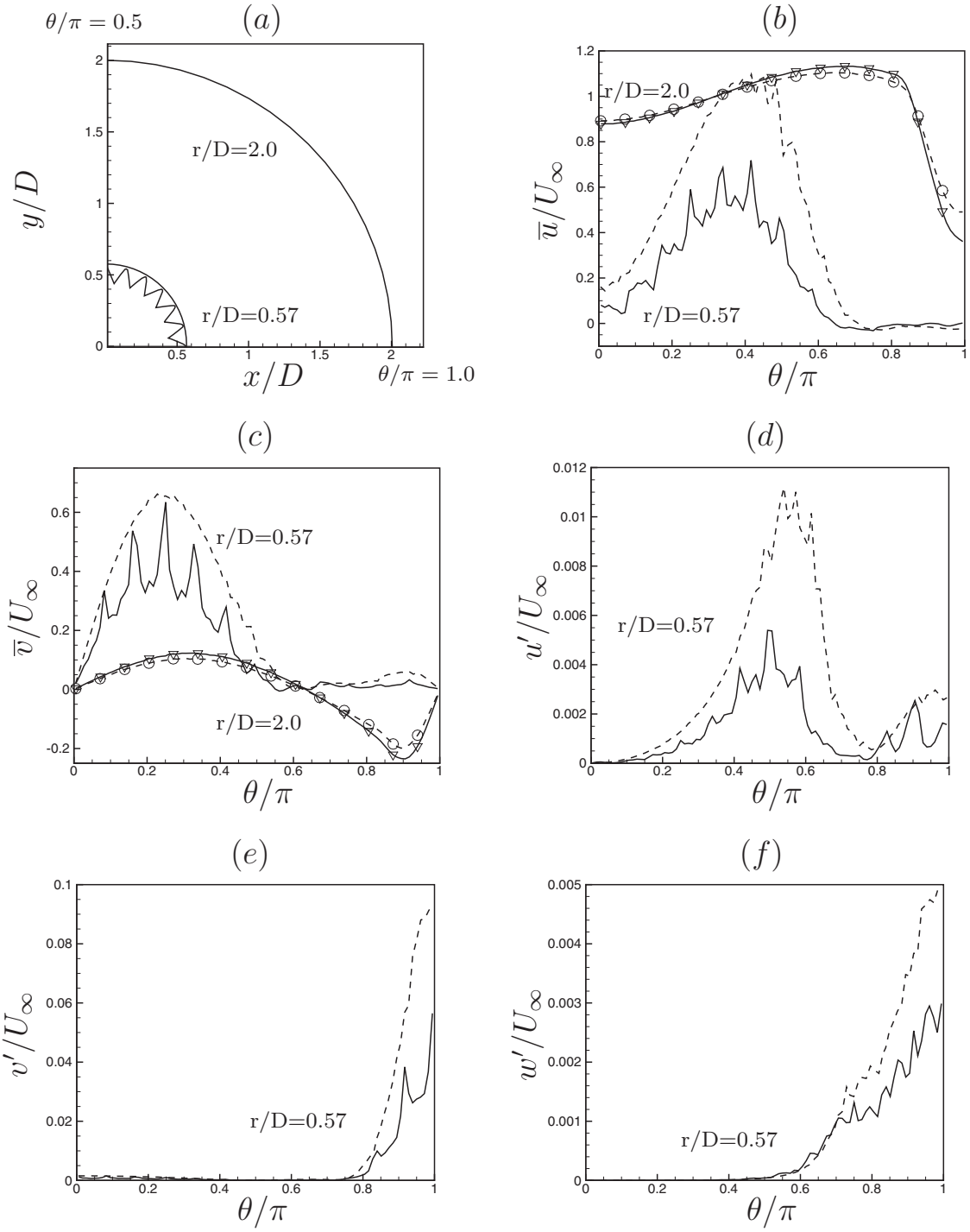

FIG. 6. Comparison of velocity statistics for Re=300. (a) Partial schematic of cactus surface showing the two azimuthal profiles corresponding to r/D=0.57 and r/D=2.0. (b) and (c) represent mean velocities along the free-stream and perpendicular to the free-stream, respectively. (d)–(f) show velocity intensities along the free-stream, perpendicular to the free-stream, and spanwise directions, respectively. For clarity only profiles in the immediate vicinity of the surface (r/D=0.57) are shown in velocity intensities. Azimuthal profiles at r/D=0.57: (—) Cactus and (---) smooth cylinder. Azimuthal profiles at r/D=2.0: (—∇) Cactus and (---○) smooth cylinder.

pressure lift increase is negligible. These competing effects dictate the overall decrease in the drag and lift coefficients, for the cactus-shaped cylinder relative to a smooth cylinder. For this particular configuration, the maximum drag coefficient decreases by about 18% and maximum lift coefficient decreases by more than 9%.

C. Re=100

The flow is transitional/turbulent at Reynolds of 300. Its turbulent nature is observed in the wake region for both geometries. The time-averaged statistics of velocity are computed in the wake region and presented in Fig. 6. These

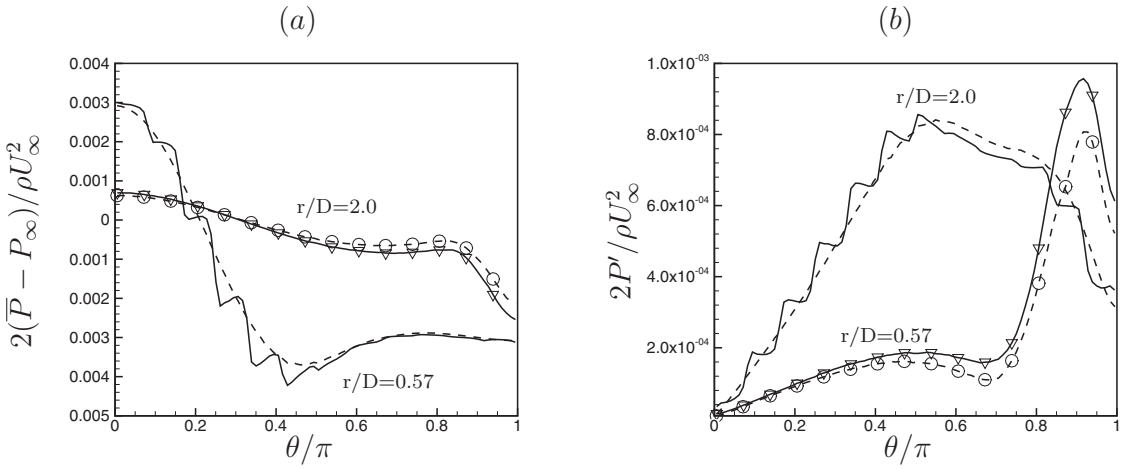

FIG. 7. Comparison of pressure statistics for Re=300. (a) Shows mean pressure and (b) shows pressure fluctuations. Refer to Fig. 6 for legends.

profiles are shown as a function of the radial distance r/D. Therefore, r/D of 0.57 is closer to the surface of the cylinders while r/D of 2.0 is closer to the free-stream. This portrayal of data allows the effect of the spikes on the near-field and free-stream to be studied. Figures 6(b) and 6(c) show that mean values of both u and v velocities for a smooth cylinder are much higher than the corresponding cactus-shaped cylinder closer to the surface. Farther away from the surface, the mean velocities for both geometries appear to collapse onto a single profile except for some difference at $\theta=\pi$. Figures 6(d)–6(f) show velocity intensities and for clarity, only profiles closer to the surface are shown. Figure 6(d) shows that the maximum intensities of u' occur around $\theta/\pi=0.5$ and the corresponding intensity for the cactus is about half that for a smooth cylinder. The v' and w' profiles in Figs. 6(e) and 6(f) show that maximum intensities for cactus-shaped cylinders occur closer to the trailing edge and their values are considerably less than those for a smooth cylinder. Statistics of the pressure field are shown in Fig. 7. The azimuthal profiles at $r/D=0.57$ and $r/D=2.0$ for mean pressure are shown in Fig. 7(a) and for fluctuating pressure in Fig. 7(b). The azimuthal profiles are seen to be different for the mean and fluctuating pressures closer to the surface. The differences are more pronounced toward the trailing edge for the azimuthal profiles at $r/D=2.0$.

Tables III and IV compare the mean and turbulent fluctuating loads between smooth and cactus-shaped cylinders. Note that the mean and the fluctuating viscous loads decrease due to the presence of spikes. Figure 8 shows the frequency spectrum of drag and lift coefficients. These frequencies are computed from the time histories of drag and lift forces on each of these cylinders. Note that a large contribution to drag and lift comes from the lower frequencies. A distinct difference between the smooth cylinder and cactus-shaped cylinder is that the presence of spikes appears to decrease the energy content in high frequencies considerably. This trend is observed for both drag coefficient [Fig. 8(a)] and lift coefficient [Fig. 8(b)].

Figure 9 shows isolines for the mean pressure around a cactus-shaped cylinder and a smooth cylinder. The flow field pattern clearly indicates that the cactus-shaped cylinder has a larger mean bubble size. If the average size of the bubble is considered from the leading edge of the cylinder, it is seen that the presence of spikes in the cactus-shaped cylinder increases the bubble size by 9.95%. The angle of separation for the cactus-shaped cylinder is 122.2° while for a smooth cylinder it is 116.05°. This behavior is consistent with the larger recirculation zone observed in a cactus-shaped cylinder.

Williamson[11] presents a detailed review of the instabilities in cylinder wakes. "Mode-A" instabilities are typically observed at lower Reynolds numbers (180–194) and are identified by larger primary vortices. In this regime, the inception of vortex loops and formation of streamwise vortex pairs are observed. These streamwise vortex pairs give rise to the larger primary vortices whose wavelengths are around 3–4 diameters. "Mode-B" instabilities are observed at higher Reynolds numbers (≈240). In this mode, there are finer scales of streamwise vortices and their spanwise length is around 1 diameter. There is a gradual transfer of energy from

TABLE III. Mean loads acting on the smooth cylinder and cactus-shaped cylinder at Re=300.

Mean data	Cylinder	Cactus	% difference
Drag coefficient (mean)	1.26	0.68	−46.03
Pressure drag (mean)	1.07	0.65	−39.25
Viscous drag (mean)	0.19	0.03	−84.21

TABLE IV. Fluctuating loads acting on the smooth cylinder and cactus-shaped cylinder at Re=300.

RMS data	Cylinder	Cactus	% difference
Drag coefficient (rms)	3.17×10^{-2}	2.5×10^{-2}	−21.08
Pressure drag (rms)	2.98×10^{-2}	2.3×10^{-2}	−19.81
Viscous drag (rms)	2.3×10^{-2}	1.1×10^{-3}	−49.56
Lift coefficient (rms)	0.44	0.23	−47.73
Pressure lift (rms)	0.41	0.23	−43.90
Viscous lift (rms)	3.3×10^{-2}	8.6×10^{-3}	−74.33

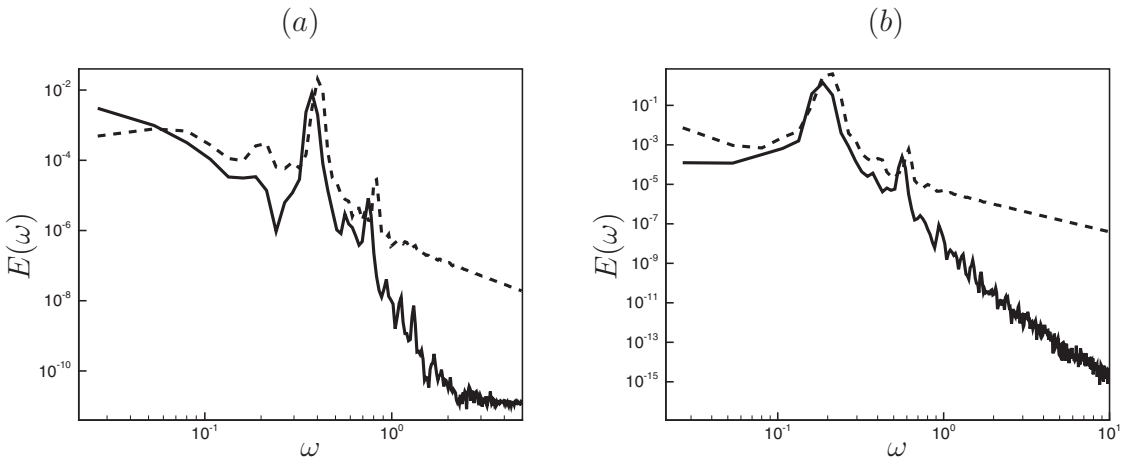

FIG. 8. Spectrum of (a) drag and (b) lift forces on the surface at Re=300. (—) Cactus-shaped cylinder and (---) smooth cylinder.

mode-A to mode-B with increasing Reynolds number. In the transition regime between $180 \leqslant \mathrm{Re} \leqslant 300$, small-scale instabilities are observed (corresponding to mode-A and mode-B) together with intermittent vortical dislocations (corresponding to mode-A* and mode-B*).

Figure 10 shows isolines of streamwise vorticity in the *X-Z* plane for both cactus-shaped and smooth cylinders. The solid isolines show positive projected vorticity values while the dashed lines indicate negative values. The nature of the vorticity fields indicates existence of both mode A and mode B three-dimensional instabilities in both geometries. This observation is in agreement with the accepted nature of smooth cylinder wakes at a Reynolds number of 300 where both modes are seen to coexist (Gushchin *et al.*[12]). It appears that although spikes alter the flow near the cylinder surface, they do not appear to change the nature of flow in the wake region. Therefore, the difference forces acting on the cactus-shaped cylinder appear to be a surface phenomenon rather than induced behavior by the wake region.

Strouhal numbers are computed at Re=100 and 300 and listed in Table V. At Reynolds number of 100, it is seen that the Strouhal number decreases by 6.25% due to the presence of spikes on the cylinder surface. At higher Reynolds number of Re=300 the Strouhal number of 0.206 for a smooth cylinder is in agreement with experimentally observed results.[13] The decrease at this higher Reynolds number is larger (10.6%) than at Re=100. The decrease in Strouhal number for cactus-shaped cylinders can be thought of as a result of the decrease in higher frequency content of the loads as shown in Fig. 8. This behavior is further substantiated by earlier results which show that mean velocity and its fluctuations, stresses (Fig. 6), pressure (Fig. 7) decrease closer to the surface due to the presence of spikes. The decrease in Strouhal number does not translate clearly into the nature of instabilities observed in a smooth cylinder and a cactus-shaped cylinder.

IV. DISCUSSION

It appears that the flow pattern near the surface changes significantly due to the presence of cavities. Figures 11(a) and 11(b) show velocity vectors within a cactus groove at Re=20 and 300, respectively. The vector plots indicate the

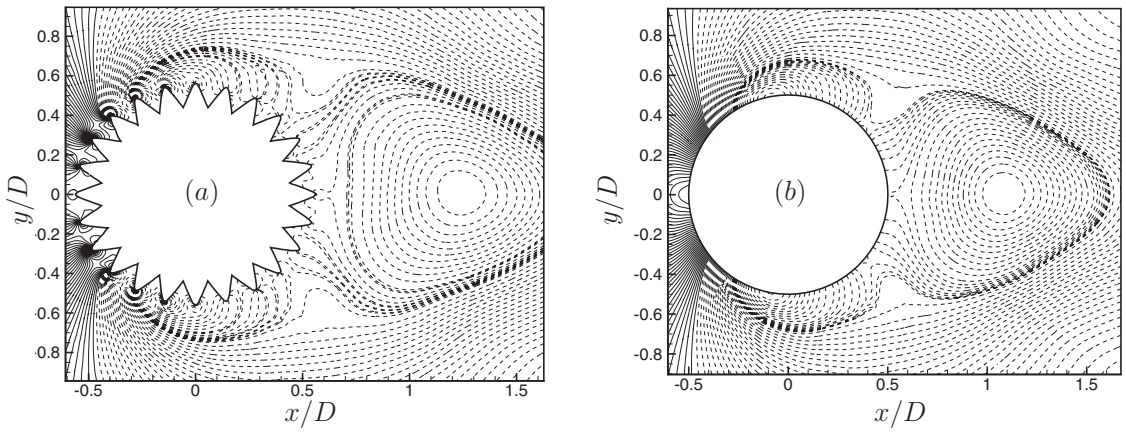

FIG. 9. Isolines of mean pressure in the vicinity of a (a) cactus-shaped cylinder and (b) smooth cylinder for a temporally averaged Re=300 flow. Solid lines indicate positive values while the dashed indicate negative values. Observe the nature of flow near spikes in the cactus-shaped geometry; this increases the mean bubble size by about 10%.

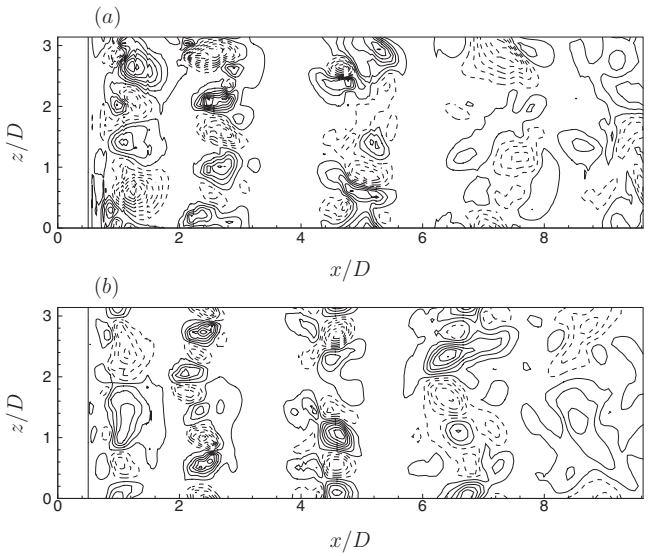

FIG. 10. Isolines of projected streamwise vorticity at Re=300. (a) Cactus-shaped cylinder and (b) smooth cylinder. Solid contours represent the positive projected streamwise vorticity while dashed isolines represent the negative values.

presence of recirculation zone(s) within the cactus grooves. Although both Figs. 11(a) and 11(b) contain recirculation zones, at Re=300 [Figs. 11(b)], we see the presence of two recirculation zones. The primary recirculation zone, which is similar to Fig. 11(a) is moved toward the free-stream and a small secondary recirculation forms in the valley closer to the surface. This indicates the presence of small-scale flow closer to the surface at high Reynolds numbers. At low Reynolds numbers the grooves create local recirculation zones filled with low momentum quiescent flow. These regions have decreased surface stresses and decreased pressure forces closer to the surface. This mechanism is absent in a smooth cylinder.

Table VI shows a comparison of viscous and pressure forces at Re=20, 100, and 300 for a smooth cylinder and a

TABLE V. Strouhal number calculations for a smooth-cylinder and a cactus shaped cylinder at Re=100 and Re=300. Observe the decrease in Strouhal number due to the presence of spikes.

Reynolds number	Cylinder	Cactus	% difference
100	0.16	0.15	−6.25
300	0.206	0.184	−10.6

cactus geometry (recompiled from results in earlier sections). For a smooth cylinder it is seen that, the viscous drag and lift forces decrease with increasing Reynolds numbers. At low Reynolds numbers (Re=20 and 100) the presence of quiescent recirculation zones within the cactus grooves lead to lower $\partial u_i/\partial x_j$ which decreases the contribution of viscous forces. As the Reynolds number increases (Re=300), smaller scales of motion are observed near the surface of cactus-shaped cylinder which lead to higher $\partial u_i/\partial x_j$. Therefore at a given Reynolds number the viscous forces decrease for a cactus-shaped cylinder in comparison to a smooth cylinder as seen in Table VI. The pressure forces do not change significantly at Re=20 and 100. At higher Reynolds number of Re=300 the pressure drag decreases by more than 39% and pressure lift decreases by more than 43% in a cactus-shaped cylinder. It is speculated that the is due to onset of three-dimensional effects. Talley and Mungal[4] observed that the forces due to a turbulent flow on a two-dimensional cylinder and free-ended cylinder are significantly different due to the presence of significant spanwise flow in a free-ended cylinder.

From the above discussions, it is speculated that the effect of drag reduction in cactus-shaped cylinders will be less pronounced at significantly higher Reynolds numbers [$\odot(10^6)$] due to the presence of smaller turbulent length scales. At these high Reynolds numbers, a turbulent flow within the cactus grooves will lead to a higher viscous forces near the surface, thereby reducing the effect of drag reduction mechanism. Since this behavior at significantly higher

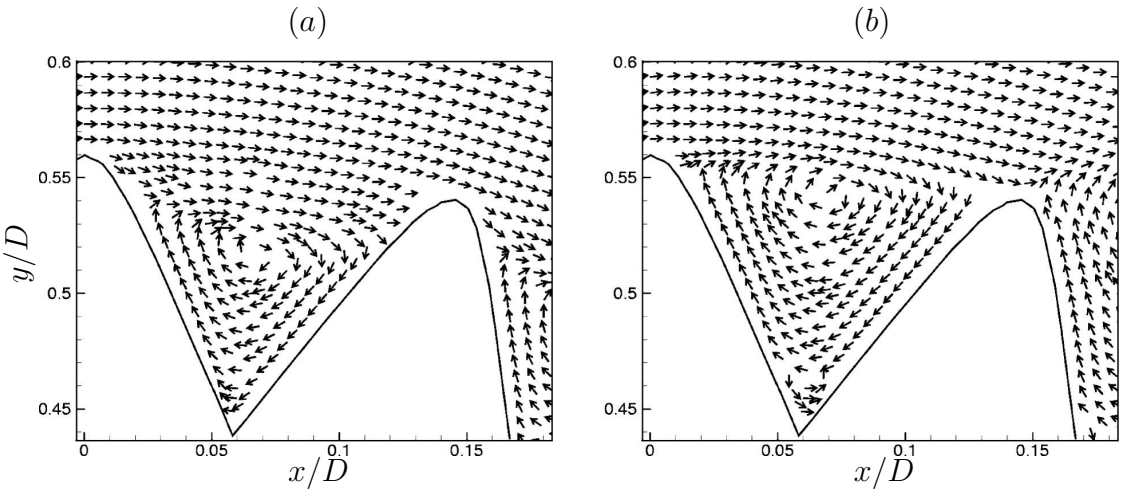

FIG. 11. Vector plot showing flow within a cactus groove at a Reynolds of (a) 20 and (b) 100. In (b), note the lift of the primary recirculation zone closer to the free-stream and the formation of a smaller secondary recirculation zone closer to the surface (in between the grooves).

TABLE VI. Comparison of viscous and pressure load coefficients acting on a smooth cylinder and cactus-shaped cylinder at different Reynolds numbers. Re=100 results correspond to maximum load. For Re=300 results, drag results correspond to mean loads while the lift results are fluctuating loads. Note that the percentage difference of these loads in cactus geometry is compared with a smooth cylinder at a given Reynolds number.

	Re=20		Re=100		Re=300	
Load coefficients	Cylinder	Cactus	Cylinder	Cactus	Cylinder	Cactus
Viscous drag	0.62	0.19	0.34	0.08	0.19	0.03
% difference		−69.35		−76.47		−84.21
Pressure drag	1.19	1.21	1.00	1.02	1.07	0.65
% difference		1.34		2.00		−39.25
Viscous lift	⋯	⋯	4.5×10^{-2}	1.5×10^{-2}	3.3×10^{-2}	8.6×10^{-3}
% difference				−66.67		−74.33
Pressure lift	⋯	⋯	0.28	0.28	0.41	0.23
% difference	⋯	⋯		0.0		−43.90

Reynolds numbers is explained based on the understanding at lower Reynolds numbers ($20 \leqslant \mathrm{Re} \leqslant 300$), the actual drag reduction mechanism might differ. Talley and Mungal[4] have performed experiments at high Reynolds numbers ($2\times10^4 \leqslant \mathrm{Re} \leqslant 2\times10^5$) for a smooth cylinder, cylinders with surface roughness, and cavities ($0 \leqslant L/D \leqslant 0.105$). Comparing a smooth cylinder and a cylinder with cavity ratio of 0.105 we have the following results from their experiments. For free-end cylinders at a Reynolds number of about 5×10^4, it is observed that there is a significant reduction in drag coefficient (about 30%) and this drag reduction decreases with an increase in Reynolds number. At a Reynolds number of 1.8×10^6, the drag reduction is only about 16%. It is therefore seen that the drag reduction is significantly higher at low Reynolds numbers and the effect decreases with increasing Reynolds number.

[1] C. Hodge, *All About Saguaros* (Hugh Harelson, Phoenix, 1991).
[2] G. N. Geller and P. S. Nobel, "Cactus ribs, influence on PAR interception and CO_2 uptake," Photosynth. Res. **107**, 482 (1984).
[3] K. J. Niklas and S. L. Buchman, "The allometry of saguaro height," Am. J. Bot. **81**, 1161 (1994).
[4] S. Talley and G. Mungal, "Flow around cactus-shaped cylinders," Annual Research Briefs, Center for Turbulence Research, NASA Ames/Stanford University, 2002, pp. 363–376.
[5] A. C. Gibson and P. S. Nobel, *The Cactus Primer* (Harvard University Press, Cambridge, 1986).
[6] P. S. Nobel, *Remarkable Agaves and Cacti* (Oxford University Press, New York, 1994).
[7] M. W. Denny, "Extreme drag forces and the survival of wind and water-swept organisms," J. Exp. Biol. **194**, 97 (1994).
[8] S. Talley, G. Iaccarino, G. Mungal, and N. Mansour, "An experimental and computational investigation of flow past cacti," Annual Research Briefs, Center for Turbulence Research, NASA Ames/Stanford University, 2001, pp. 51–63.
[9] K. Mahesh, G. Constantinescu, and P. Moin, "A numerical method for large-eddy simulation in complex geometries," J. Comput. Phys. **197**, 215 (2004).
[10] F. Nieuwstadt and H. B. Keller, "Viscous flow past circular cylinders," Comput. Fluids **1**, 59 (1973).
[11] C. H. K. Williamson, "Vortex dynamics in the cylinder wake," Annu. Rev. Fluid Mech. **28**, 477 (1996).
[12] V. A. Gushchin, A. V. Kostomarov, P. V. Matyushin, and E. R. Pavlyukova, "Direct numerical simulation of the transitional separated fluid flows around a sphere and a circular cylinder," J. Wind. Eng. Ind. Aerodyn. **90**, 341 (2002).
[13] C. H. K. Williamson, "The natural and forced formation of spot-like dislocations in the transition of a wake," J. Fluid Mech. **243**, 393 (1992).